

# Quantum confinement and surface relaxation effects in rutile TiO<sub>2</sub> nanowires

Abraham Hmiel and Yongqiang Xue\*

College of Nanoscale Science and Engineering, State University of New York, Albany, New York 12203, USA

(Received 15 November 2011; revised manuscript received 27 April 2012; published 28 June 2012)

Spin-polarized density functional theory calculations within the generalized gradient approximation have been applied to investigate the size- and shape-dependent atomic and electronic properties of [001]-oriented rutile TiO<sub>2</sub> nanowires of rectangular cross section. We find pronounced even-odd oscillation in the formation energy and band structure of the nanowires as a function of the number of TiO<sub>2</sub> layers, which are largely connected to the presence or absence of a mirror Ti-O plane along either confinement direction. We demonstrate that the relative stability and the oscillation in the band structure characters of the rutile TiO<sub>2</sub> nanowires arise from the interplay between surface relaxation and quantum confinement effects, which depend on the even-odd parity of the number of TiO<sub>2</sub> layers and can be tuned separately along each confinement direction.

DOI: [10.1103/PhysRevB.85.235461](https://doi.org/10.1103/PhysRevB.85.235461)

PACS number(s): 73.22.-f, 78.67.Uh, 81.07.Gf

## I. INTRODUCTION

Titanium dioxide (TiO<sub>2</sub>) is an important material for heterogeneous catalysis and photocatalysis, and has been widely used as a model system for fundamental surface science study of oxide materials.<sup>1-3</sup> With the advent of nanotechnology, TiO<sub>2</sub> nanowires in different crystalline order have been exploited in a wide range of applications including dye-sensitized solar cells, proton-exchange-membrane fuel cells, and gas sensors.<sup>4,5</sup> The majority of these applications have focused on nanowires with diameters of tens of nanometers. The recent developments in the synthesis of TiO<sub>2</sub> nanowires with diameters on the atomic scale<sup>6</sup> have opened up new grounds for studying structure-property relationships in the regime where quantum confinement effects are important. In the subnanometer range, the properties of nanowires can be sensitive to atomic-level control of surface morphology, functionalization, and nanowire stoichiometry during the growth and fabrication processes, thereby opening the way for new applications.

Relatively few theoretical studies on atomic-scale TiO<sub>2</sub> nanowires in either rutile or anatase structures have been published.<sup>7-15</sup> In particular, two recent studies<sup>14,15</sup> have shown that the stability and electronic properties of TiO<sub>2</sub> nanowires are sensitive to the nanowire orientation, the presence of screw symmetry, and the size of the nanowires. Both works have focused on nanowires with square cross section. In this paper, we attempt to shed new light on the structure-property relationship in these novel one-dimensional (1D) nanomaterials by presenting a systematic density functional theory (DFT) study on the size- and shape-dependent atomic and electronic properties of rutile TiO<sub>2</sub> nanowires with rectangular cross section of different size and aspect ratio.

The TiO<sub>2</sub> nanowires studied correspond to those cut along the [001] direction of the bulk rutile crystal and enclosed by the {110} facets, which are the most stable facets for [001]-oriented rutile nanowires.<sup>12,14</sup> We use the notation  $m \times n$  to classify these stoichiometric nanowires of rectangular cross section, where the two indices  $m$  and  $n$  characterize the number of TiO<sub>2</sub> layers parallel to the facets along each lateral dimension. The examples of  $6 \times 8$ ,  $5 \times 8$ , and  $3 \times 7$  nanowires are shown in Fig. 1. We note that the TiO<sub>2</sub> layer is composed of a mixed Ti-O plane with an equal number of Ti and O atoms sandwiched between two layers of O atoms. At the (110)

surface, rows of sixfold coordinated Ti atoms (Ti-6c) alternate with rows of fivefold coordinated Ti atoms (Ti-5c) along the [001] direction. The bridging O atoms in the outermost layer are twofold coordinated (O-2c), while all other O atoms are threefold coordinated (O-3c) as in the bulk (Fig. 1).

The bulk rutile TiO<sub>2</sub> crystal belongs to the space group  $P4_2/mnm$ .<sup>1</sup> For square  $m \times m$  rutile nanowires oriented along the [001] direction, we can identify two rotational axes parallel to the nanowire axis:<sup>15</sup> one fourfold screw axis going through the interstitial region in the middle of the concentric squares of Ti atoms for an *even* number of  $m$  and one twofold axis going through the Ti atoms for an *odd* number of  $m$ . Recent studies<sup>14,15</sup> have shown that the presence or absence of the screw axis in the square nanowires is coupled to the indirect or direct character of the band structure, with the  $m \times m$  nanowire with odd (even)  $m$  having direct (indirect) band gap. In addition, square wires with screw symmetry have been found to possess consistently lower formation energy and higher band gap than square wires without it.<sup>14,15</sup>

However, for general  $m \times n$  nanowires, this simple classification no longer applies, as the nanowires possess different reduced symmetry depending on the even-odd parity of  $m$  and  $n$ . We show instead that the key element determining the difference in electronic properties of rectangular nanowires is the presence (*when  $m$  or  $n$  is odd*) or absence (*when  $m$  or  $n$  is even*) of a mirror Ti-O plane in either confinement direction, with the square nanowires being a special case of the general classification. In addition, if both  $m$  and  $n$  are odd and  $m \neq n$ , two different ways of constructing nanowires exist that are not related to symmetry but depend on whether the mirror Ti-O plane terminates on the sixfold (Ti-6c) or fivefold (Ti-5c) coordinated Ti atoms at the facet surfaces along each confinement direction. The example of  $3 \times 7$  nanowire is shown in Fig. 1(B). We find that the differences in the electronic properties of these rectangular nanowires are a direct consequence of the different surface relaxations occurring along each lateral confinement direction as a function of the corresponding number ( $m$  or  $n$ ) of TiO<sub>2</sub> layers.

The importance of the even-odd parity of the number of TiO<sub>2</sub> layers in determining the electronic properties of ultrathin rutile TiO<sub>2</sub>(110) films was first recognized by Bredow *et al.*<sup>16</sup>

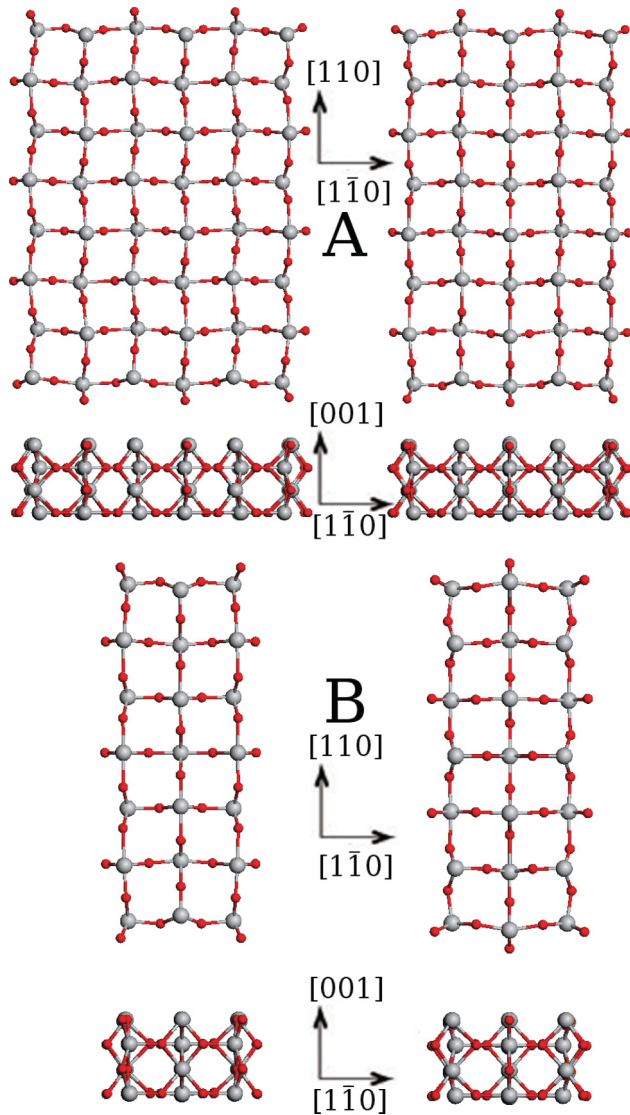


FIG. 1. (Color online) Atomic structures of the  $6 \times 8$  (left figure in A),  $5 \times 8$  (right figure in A),  $3 \times 7_1$  (left figure in B), and  $3 \times 7_2$  (right figure in B) rutile  $\text{TiO}_2$  nanowires oriented along the  $[001]$  direction. For the type-1  $3 \times 7_1$  nanowire, the mirror Ti-O plane along the first confinement direction terminates on the Ti-5c atoms at the corresponding facet surfaces. For the type-2  $3 \times 7_2$  nanowire, the mirror Ti-O plane instead terminates on the surface Ti-6c atoms which are bound to the twofold coordinated bridging O atoms (O-2c). The large gray and small red spheres represent Ti and O atoms, respectively. For each nanowire, both the axial view (upper figure) and side view (lower figure) are shown.

It has also been extensively studied in the context of slab model calculations of the rutile  $\text{TiO}_2(110)$  surface, mainly to determine the number of layers that are needed to obtain a reliable description of surface and adsorption properties.<sup>17–23</sup> In this paper we show that the ability to tune separately the number of  $\text{TiO}_2$  layers along two confinement directions leads to additional subtle and interesting effects arising from the interplay between surface relaxation and quantum confinement in rutile  $\text{TiO}_2$  nanowires.

## II. COMPUTATIONAL METHODS

Our first-principles density functional theory (DFT) calculations are performed using the SIESTA code<sup>24</sup> with norm-conserving pseudopotential.<sup>25</sup> Either the Perdew-Burke-Ernzerhof (PBE) parametrization<sup>26</sup> within the generalized gradient approximation (GGA) or the Perdew-Zunger parametrization<sup>27</sup> within the local-density approximation (LDA) of the exchange-correlation functional have been employed. The pseudopotentials used in this calculation were generated using the ATOM program<sup>28</sup> with the corresponding DFT functionals. In the pseudopotential generation procedure, the valence electron configuration was chosen to be  $3s^23p^63d^2$  for Ti and  $2s^22p^4$  for O, while the cutoff radii for the  $[s,p,d,f]$  angular momentum channels were 1.30, 1.30, 1.30, 1.98 Bohr and 1.14, 1.14, 1.14, 1.14 Bohr for Ti and O, respectively. All calculations are spin polarized using the optimized double- $\zeta$  plus polarization (DZP) basis set and a real-space mesh cutoff of 570 Ry. The cutoff radii and soft-confinement parameters for the numeric orbital basis functions of Ti and O were obtained by minimizing the Harris energy in the bulk rutile  $\text{TiO}_2$  crystal in a multistep approach using the simplex method<sup>29</sup> as implemented within the SIESTA code.<sup>24,30</sup>

Benchmark calculations were first performed on the bulk rutile crystal of  $\text{TiO}_2$ , which was relaxed to its ground state with a  $12 \times 12 \times 16$  Monkhorst-Pack  $k$ -point mesh<sup>31</sup> and a maximum force tolerance of  $0.008 \text{ eV}/\text{\AA}$ , from which we obtain bulk lattice parameters of  $a = 4.657 \text{ \AA}$ ,  $c = 2.989 \text{ \AA}$ ,  $u = 0.304$ , which compare well with both the experimental values<sup>32,33</sup> and results from previous DFT calculations<sup>16,17,19,23,34,35</sup> using plane-wave (PW) basis set and the projector augmented wave (PAW) or linearized augmented plane-wave (LAPW) methods. The results are summarized in Table I. The bulk indirect and direct band gaps are found to be 1.78 and 1.82 eV, respectively, in good agreement with previous DFT calculations but being significantly smaller than the experimental values.<sup>32,36,37</sup> We note that this well-known underestimation of band gap in the current DFT-GGA functionals<sup>38</sup> can be corrected within the quasiparticle approach using the self-consistent GW approximation,<sup>39</sup> as shown in a recent study on bulk rutile  $\text{TiO}_2$ .<sup>40</sup> However, due to its large computational cost, similar studies on  $\text{TiO}_2$  nanowires have not been reported in the literature. The present investigation may serve as a useful qualitative guide to the more rigorous (and more expensive) quasiparticle calculations.

A further benchmark test was performed on the rutile (110)  $\text{TiO}_2$  surface constructed from the optimized bulk structure. Using a slab model composed of 3–7  $\text{TiO}_2$  layers with either one or two bottom layers fixed at the corresponding bulk positions, we were able to reproduce the well-known even-odd oscillation in surface energy and band gap with respect to the number of  $\text{TiO}_2$  layers, with the relaxed bond lengths in the surface and subsurface layers and interlayer distances being in good agreement with those documented in literature.<sup>16,20–23</sup> In particular, the work function of the rutile (110) surface computed using a six-layer slab model<sup>41</sup> is found to be 6.49 eV in PBE-GGA, compared with the values ( $\sim 7.2 \text{ eV}$ ) reported for plane-wave PAW calculation in Ref. 22. This underestimation of work function is consistent with the recent

TABLE I. Benchmark comparison of lattice parameters  $a$  and  $c$ , structural parameter  $u$ , and direct band gap at the  $\Gamma$  point (indirect band gap in parentheses) for bulk rutile crystal of  $\text{TiO}_2$  between our linear-combination-of-atomic-orbital (LCAO) calculation and selected theoretical and experimental studies.

Method	$a$ (Å)	$c$ (Å)	$u$	Band gap (eV)
LCAO-PBE (this work)	4.657	2.989	0.304	1.82 (1.78)
LCAO-LDA (this work)	4.551	2.953	0.304	1.76
PW-PW91 <sup>a</sup>	4.658	2.977	0.305	1.75
PW-PW91 <sup>b</sup>	4.639	2.976	0.305	
PAW-PBE <sup>b</sup>	4.594	2.959	0.306	
PAW-PBE <sup>c</sup>	4.647	2.974	0.305	1.69
PAW-LDA <sup>c</sup>	4.557	2.928	0.304	1.67
LAPW-PBE <sup>d</sup>	4.622	2.958	0.305	2.00
LAPW-LDA <sup>d</sup>	4.563	2.939	0.304	2.00
PW-PBE <sup>e</sup>	4.649	2.966	0.305	1.86
Experiment <sup>f</sup>	4.594	2.958	0.305	3.05 (2.95)

<sup>a</sup>Reference 16.  
<sup>b</sup>Reference 22.  
<sup>c</sup>Reference 34.  
<sup>d</sup>Reference 35.  
<sup>e</sup>Reference 23.  
<sup>f</sup>References 32,33.

study in Ref. 30 on the accuracy of strictly localized atomic orbital bases in describing surface properties, considering the fact that the work function is sensitive to the long-range tails of wave-function decay in the vacuum region.

With the validity of our computational setup verified, we performed a systematic study on the atomic and electronic properties of a series of rectangular [001]-oriented rutile  $\text{TiO}_2$  nanowires with cross-sectional areas between 0.2 and 4.8  $\text{nm}^2$  (defined through the four bridging O atoms at the corner; see Fig. 1), corresponding to the number of  $\text{TiO}_2$  layers  $m$  and  $n$  ranging from 3 to 8. The nanowire structure is considered fully relaxed if the force on any atom is reduced below 0.016 eV/Å. The lattice constant along the nanowire axis (chosen as the  $z$  axis) is optimized by minimizing the uniaxial stress. The supercell sizes were chosen to give a vacuum region of at least 1.3 nm in the lateral directions between the image nanowires. This spacing between the nanowire images ensures an energy convergence of less than 0.1 meV per atom. The 1D Brillouin zone was sampled using a  $1 \times 1 \times 16$  Monkhorst-Pack  $k$ -point mesh. The total energy convergence threshold is set at  $1 \times 10^{-4}$  eV.

### III. RESULTS AND DISCUSSION

#### A. Structure and energetics

We report in this section trends in the dependence of nanowire structural and energetic properties on the number of  $\text{TiO}_2$  layers in each confinement direction. Due to their small size, the nanowires undergo significant relaxation in both the surface and interior layers. Along each confinement direction, the deviation from the bulklike termination follows a general pattern depending on the even-odd parity of the number of  $\text{TiO}_2$  layers ( $m$  or  $n$ ), similar to that observed in the  $\text{TiO}_2(110)$  thin films.<sup>16</sup> This is illustrated in Tables II–V, where we show the interlayer distances along both confinement directions for the four nanowire series. The interlayer distances are defined

through the average distance between the Ti atoms facing each other on neighboring  $\text{TiO}_2$  layers.<sup>16</sup>

For all the nanowires studied except for the smallest  $2 \times n$  and  $3 \times n$  nanowires, the first and second  $\text{TiO}_2$  layers are separated by a distance ranging from 3.28 to 3.31 Å, slightly longer than the bulk value of 3.27 Å. If the number of layers ( $m$  or  $n$ ) along any confinement direction are even, the distance between the second and third layers becomes considerably larger by at least 0.08 Å and up to 0.14 Å. This oscillation in interlayer distance persists into the interior of the larger nanowires, albeit with reduced magnitude. As a result, the nanowire can be considered as composed of a series of bilayers with the first two surface layers weakly bound to the rest along the corresponding confinement direction. In contrast, when  $m$  or  $n$  are odd, no oscillation in the interlayer distance is observed. Although the distance between the second and third

TABLE II. Interlayer distances (Å) along both confinement directions for  $m \times n$   $\text{TiO}_2$  nanowires where both  $m$  and  $n$  are even

$m \times n$	Interlayer distance (Å)							
$2 \times 2$	3.28							
	3.29							
$2 \times 4$	3.34							
	3.30	3.43	3.30					
$4 \times 4$	3.30	3.45	3.30					
	3.31	3.45	3.31					
$4 \times 6$	3.31	3.47	3.30					
	3.32	3.40	3.29	3.40	3.30			
$4 \times 8$	3.31	3.48	3.31					
	3.30	3.38	3.29	3.35	3.29	3.38	3.30	
$6 \times 6$	3.30	3.41	3.29	3.41	3.30			
	3.30	3.41	3.29	3.40	3.31			
$6 \times 8$	3.30	3.41	3.28	3.41	3.30			
	3.30	3.39	3.28	3.36	3.28	3.39	3.30	

TABLE III. Interlayer distances (Å) along both confinement directions for  $3 \times n$  TiO<sub>2</sub> nanowires.

$m \times n$	Interlayer distance (Å)					
$3 \times 2$	3.29	3.29				
	3.35					
$3 \times 3$	3.23	3.23				
	3.35	3.35				
$3 \times 4$	3.31	3.31				
	3.35	3.49	3.30			
$3 \times 5_1$	3.27	3.27				
	3.33	3.34	3.34	3.33		
$3 \times 5_2$	3.31	3.31				
	3.27	3.33	3.32	3.27		
$3 \times 6$	3.29	3.29				
	3.34	3.43	3.29	3.44	3.28	
$3 \times 7_1$	3.31	3.31				
	3.28	3.36	3.29	3.29	3.36	3.28
$3 \times 7_2$	3.27	3.27				
	3.34	3.38	3.31	3.31	3.38	3.34

layers is still larger than that between the first and second layers, the difference is reduced compared to that of even  $m$  or  $n$ . This trend is consistent with previous studies on rutile TiO<sub>2</sub>(110) thin films.<sup>16</sup>

The key element distinguishing the nanowires with odd number of TiO<sub>2</sub> layers from the even ones is the presence of a mirror Ti-O plane, which ensures the center TiO<sub>2</sub> layer not being skewed as shown in Fig. 1. If either  $m$  or  $n$  is odd, pairs of surface Ti-5c or Ti-6c atoms exist that face each other on the opposite facets along the corresponding confinement direction. Since the Ti-5c (Ti-6c) atoms on the rutile (110) surface tends to relax inward (outward), surface relaxations on opposite facets tend to interfere with each other. This is not the case when  $m$  or  $n$  is even, where we find pairs of Ti-5c and Ti-6c atoms facing each other on the opposite facets.

The changes in the energetic and electronic properties of the rectangular nanowires are a direct consequence of the different structural rearrangements occurring in the nanowires as a function of the number of TiO<sub>2</sub> layers  $m$  and  $n$  along each confinement direction. The trends in the formation energies

TABLE IV. Interlayer distances (Å) along both confinement directions for  $5 \times n$  TiO<sub>2</sub> nanowires.

$m \times n$	Interlayer distance (Å)					
$5 \times 4$	3.29	3.32	3.32	3.29		
	3.33	3.50	3.30			
$5 \times 5$	3.28	3.32	3.32	3.28		
	3.31	3.34	3.34	3.31		
$5 \times 6$	3.30	3.32	3.33	3.30		
	3.29	3.44	3.30	3.43	3.33	
$5 \times 7_1$	3.29	3.33	3.33	3.28		
	3.32	3.36	3.30	3.30	3.36	3.32
$5 \times 7_2$	3.31	3.35	3.35	3.31		
	3.28	3.36	3.28	3.28	3.37	3.28
$5 \times 8$	3.29	3.33	3.33	3.29		
	3.30	3.42	3.29	3.38	3.29	3.32

TABLE V. Interlayer distances (Å) along both confinement directions for  $7 \times n$  TiO<sub>2</sub>. Note that the  $7 \times 5_{1,2}$  nanowires are rotationally equivalent to the  $5 \times 7_{1,2}$  nanowires.

$m \times n$	Interlayer distance (Å)					
$7 \times 4$	3.29	3.34	3.29	3.29	3.34	3.29
	3.30	3.48	3.32			
$7 \times 5_1$	3.32	3.36	3.30	3.30	3.36	3.32
	3.29	3.33	3.33	3.29		
$7 \times 5_2$	3.28	3.36	3.28	3.28	3.37	3.28
	3.31	3.35	3.35	3.31		
$7 \times 6$	3.30	3.35	3.29	3.35	3.30	
	3.30	3.44	3.29	3.43	3.31	
$7 \times 7$	3.29	3.36	3.29	3.29	3.36	3.29
	3.31	3.37	3.30	3.30	3.37	3.31

are shown in Fig. 2, where we show also the optimized lattice constant  $c$  along the nanowire axis. The formation energies determine the relative stability of the nanowires compared to the bulk rutile phase of TiO<sub>2</sub> and are computed from  $E_{\text{form}} = (E_{\text{NW}} - \mu_{\text{TiO}_2} n_{\text{TiO}_2}) / n_{\text{TiO}_2}$ , where  $E_{\text{NW}}$  and  $n_{\text{TiO}_2}$  are the total energy and number of TiO<sub>2</sub> units in the nanowires, respectively.  $\mu_{\text{TiO}_2}$  is the chemical potential of a TiO<sub>2</sub> unit in the bulk rutile crystal. Note that we have neglected the vibrational contributions to the formation energy, because their effects were found to be small from a previous study on square nanowires.<sup>15</sup>

If both  $m$  and  $n$  are even, the formation energy of the  $m \times n$  nanowires decreases monotonically with increasing perimeter and cross-sectional area. The other nanowires corresponding to  $m = 3, 5, 7$  show even-odd oscillation with respect to the number of TiO<sub>2</sub> layers  $n$  along the other confinement direction, with the formation energy of the  $3 \times n$  series of nanowires being significantly larger. This is consistent with previous study of rutile TiO<sub>2</sub>(110) thin films,<sup>16</sup> where the surface energy of a three-layer film is found to be significantly larger than that of other thin films. If we specialize to the square  $m \times m$  nanowires, we observe strong even-odd oscillation in formation energy with respect to  $m$  with the nanowires with screw symmetry (even  $m$ ) being consistently more stable, in agreement with previous studies.<sup>14,15</sup> In contrast, the axial lattice constant  $c$  increases toward the bulk value with similar functional dependence on the perimeter and cross-sectional area for all nanowires studied, although the  $3 \times n$  nanowires have consistently smaller lattice constant than other nanowires of similar cross-sectional area and perimeter (Fig. 2).

## B. Band structure

We report in this section trends in the dependence of nanowire band structures on the number of TiO<sub>2</sub> layers in each confinement direction. The computed band gaps and conduction-/valence-band edges using PBE-GGA functional are shown in Fig. 3 as a function of both the nanowire perimeter<sup>42</sup> and cross-sectional area. The band edges are aligned by lining up the Fermi levels of all the nanowires studied, which are chosen as the energy reference. Three distinct trends can be identified. First, if both  $m$  and  $n$  are even, the corresponding nanowires have  $C_{2h}$  symmetry and

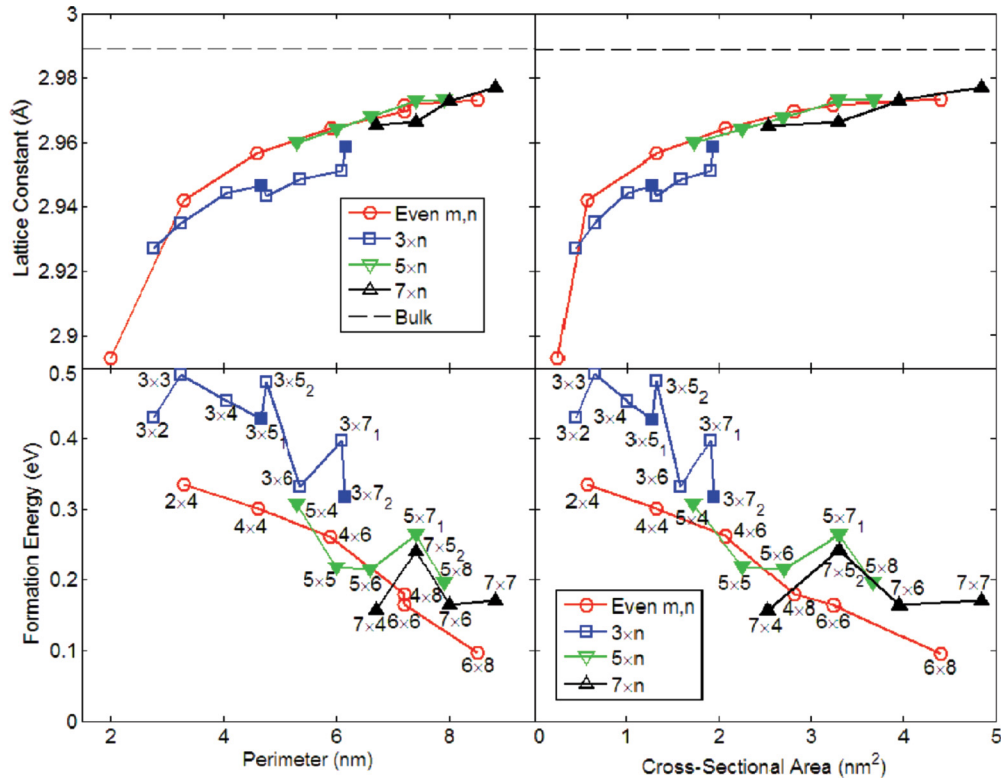


FIG. 2. (Color online) The upper figures show the dependence of the axial lattice constant on the perimeter (left) and cross-sectional area (right) with the PBE functional. The horizontal line denotes the corresponding bulk value. The lower figures show the formation energy per  $\text{TiO}_2$  unit as a function of the perimeter (left) and cross-sectional area (right). In all figures, the filled markers denote a direct band gap at the  $\Gamma$  point and empty markers denote an indirect gap.

possess an indirect band structure with the band gap decreasing monotonically toward the bulk value with increasing cross-sectional area (perimeter). The reduction in band gap is accomplished by both a decrease in conduction-band edge and increase in the valence-band edge as expected from simple quantum confinement consideration. From the computed band structure, we find that the valence-band maximum (VBM) is located at the  $\Gamma$  point, while the conduction-band minimum (CBM) shifts gradually from nearly  $(0,0,0.5)$  for the smallest  $2 \times 2$  nanowire to nearly  $(0,0,0.4)$  for the largest  $6 \times 8$  nanowire along the  $\Gamma$ - $X$  direction in the 1D Brillouin zone. In comparison, the conduction-band minimum in the bulk rutile crystal is located at the  $M$  points with a  $k$  vector of  $(\frac{1}{2}, \frac{1}{2}, 0)$  and equivalent.

Second, for  $3 \times n$  nanowires with the smallest odd number of  $\text{TiO}_2$  layers along the first confinement direction, both indirect and direct band structures are observed. Note that for *odd*  $n$  and  $n \neq 3$ , there are two ways to construct stoichiometric rutile  $3 \times n$  (in general, also for odd  $m \times n$  nanowires with  $m \neq n$ ) nanowires that are not related to symmetry. The example of the  $3 \times 7$  nanowire has been shown in Fig. 1(B). For the type-1  $3 \times 7_1$  nanowire, the mirror Ti-O plane along the first confinement direction terminates on the Ti-5c atoms at the corresponding facet surfaces. For the type-2  $3 \times 7_2$  nanowire, the mirror Ti-O plane instead terminates on the surface Ti-6c atoms which are bound to the twofold coordinated bridging O atoms (O-2c). This seemingly trivial difference in structure can lead to a significant change in the electronic structure, as

we find that the type-2  $3 \times n$  nanowires possess direct band structure, with both CBM and VBM located at the  $\Gamma$  point. In contrast, all other  $3 \times n$  nanowires possess indirect band structure, with the CBM located at the  $\Gamma$  point and the VBM shifted toward the  $X$  point.

Finally, the  $5 \times n$  and  $7 \times n$  nanowires possess a direct band structure with both CBM and VBM located at the  $\Gamma$  point, for both even and odd  $n$  and for both types of surface termination schemes when  $n$  is odd. Overall an even-odd oscillation can still be observed in the computed band gap for the  $3 \times n$ ,  $5 \times n$ , and  $7 \times n$  nanowires depending on the number of  $\text{TiO}_2$  layers  $n$  along the second confinement direction. However, the changes in the conduction-band and valence-band edges are similar with increasing perimeter and cross-sectional area (Fig. 3).

If we consider again only the cases of square  $m \times m$  nanowires, the computed band gaps show strong even-odd oscillations with respect to  $m$ , with the nanowires with screw symmetry (even  $m$ ) being indirect and having consistently larger band gap, which are also observed in previous studies.<sup>14,15</sup> The convergence of the computed band gap towards bulk value with increasing number of layers is rather slow and far from being completed for the nanowires studied here, which is consistent with previous studies on rutile  $\text{TiO}_2(110)$  thin films and surfaces<sup>16,20-23</sup> but differs from that in Ref. 14 where the convergence toward bulk value is already achieved around  $m = 8$ . We note that a significantly smaller real-space mesh cutoff (150 Ry) is used in Ref. 14 than that used here (570 Ry).

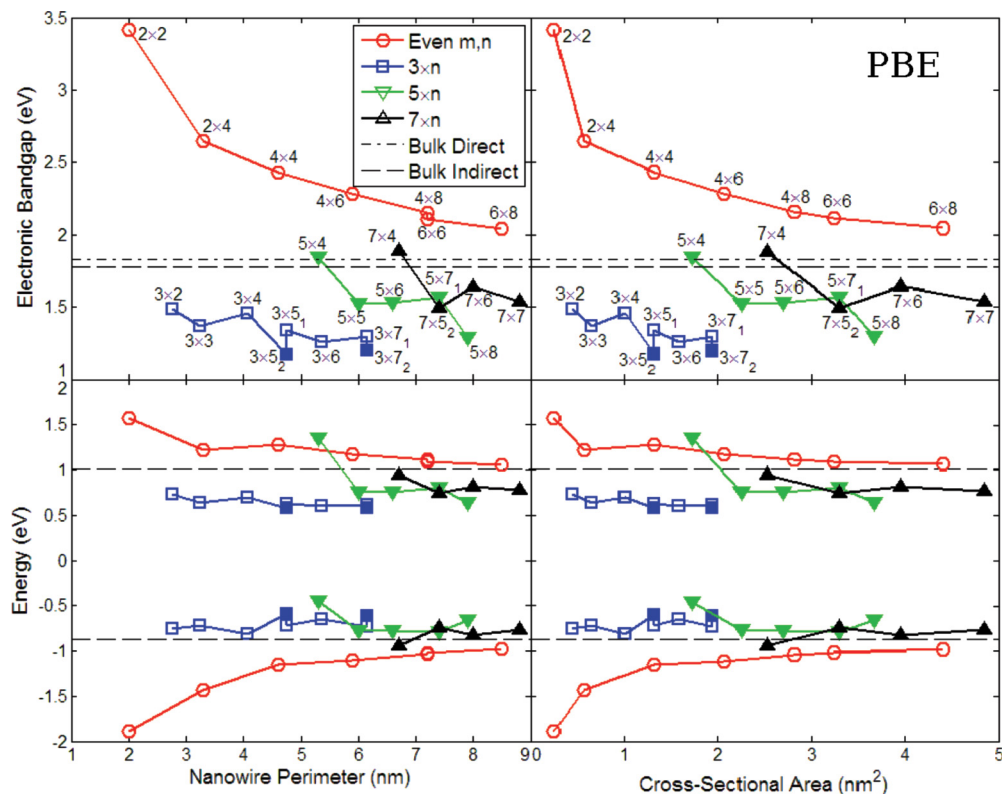


FIG. 3. (Color online) Dependence of the band gap (upper figures) and the conduction- and valence-band edges (lower figures) of the rectangular rutile  $\text{TiO}_2$  nanowires on the perimeter (left figures) and cross-sectional area (right figures). The band edges are aligned by lining up the Fermi levels of the different nanowires, which are chosen as the energy reference. In all figures, the filled markers denote a direct band gap at the  $\Gamma$  point and empty markers denote an indirect gap. The two horizontal lines in the band-gap plot show the bulk indirect and direct band gaps, respectively. The two horizontal lines in the band-edge plot show the positions of the bulk conduction- and valence-band edges relative to the bulk Fermi level (set at the energy reference).

Since the computed band structures may be sensitive to the choice of exchange-correlation functionals, a spin-polarized LDA calculation with the corresponding pseudopotentials has also been performed for all the nanowires studied at the PBE relaxed geometries. We note that such LDA band structures often form the basis for the more rigorous quasiparticle calculation.<sup>39,40</sup> The results are shown in Fig. 4. We find that the absolute difference in the band gap between the PBE and LDA calculations typically ranges from 0.01 to 0.07 eV. And for the nanowires studied, the choice of PBE or LDA functionals does not affect the trends in band-structure character as a function of either nanowire perimeter or cross-sectional area (Fig. 4).

### C. Density of states and orbital interaction analysis

To provide a deeper understanding into the electronic origin of the structural changes with the number of layers and its effect on the direct and indirect character of the nanowires, we analyze the band structure through the density of states projected onto the  $3d$  and  $2p$  orbitals of the surface Ti and O atoms (PDOS) in Fig. 5, the nature of the wave functions at the conduction- and valence-band edges through the spatial distribution of the local density of states (LDOS) in Figs. 6 and 7, and the orbital interaction within the nanowire through the crystal orbital overlap population (COOP)<sup>43</sup> in Fig. 8 for selected nanowires along both confinement directions. Note

that the crystal orbital overlap population is essentially the density of states weighted with the overlap population of the corresponding crystal orbitals, the positive, negative, and zero values of which denote bonding, antibonding, and nonbonding characters between the selected orbitals at the corresponding energy.<sup>43</sup>

The plot of the PDOS is shown in Fig. 5 for the  $6 \times 8$   $\text{TiO}_2$  nanowire, where we find that the conduction-band states are contributed predominantly by the  $3d$  orbitals of Ti atoms, while the valence states arise primarily from the  $2p$  orbitals of O atoms with some mixing from the  $3d$  orbitals of Ti atoms. For the even  $6 \times 8$  nanowire, the surface PDOS plots along both confinement directions are qualitatively similar to that obtained from slab model calculation of rutile  $\text{TiO}_2(110)$  surface with an even number of layers.<sup>23</sup>

From the LDOS plots of the  $6 \times 8$  nanowire in Fig. 6(A), we find clearly the signature of the formation of bilayers within the nanowire along both confinement directions. The spatial distribution of the wave functions at both conduction- and valence-band edges are nearly identical moving along each confinement direction. The state at the conduction-band edge is mainly contributed by the  $3d$  orbitals of the surface Ti-5c atoms and the neighbor subsurface Ti-6c atoms, the tails of which penetrate into the interior of the nanowire. The state at the valence-band edge is contributed mainly by the  $2p$  orbitals of the threefold coordinated O atoms (O-3c) and is delocalized

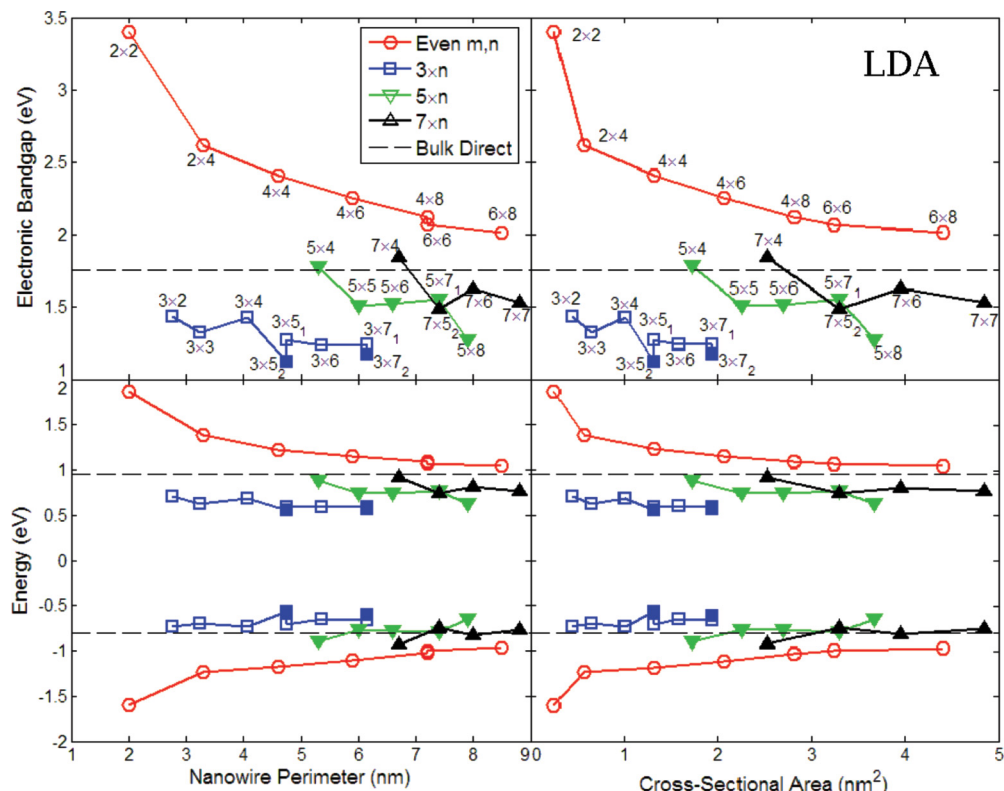


FIG. 4. (Color online) Dependence of the band gap (upper figures) and the conduction- and valence-band edges (lower figures) of the rectangular rutile TiO<sub>2</sub> nanowires on the perimeter (left figures) and cross-sectional area (right figures) computed at the PBE relaxed geometries using the LDA exchange-correlation functional and corresponding pseudopotentials, similar to those shown in Fig. 3.

throughout the nanowire. Due to the small size of the nanowire, both surface and interior atoms contribute to the total DOS as shown in the LDOS plot of Fig. 6(A).

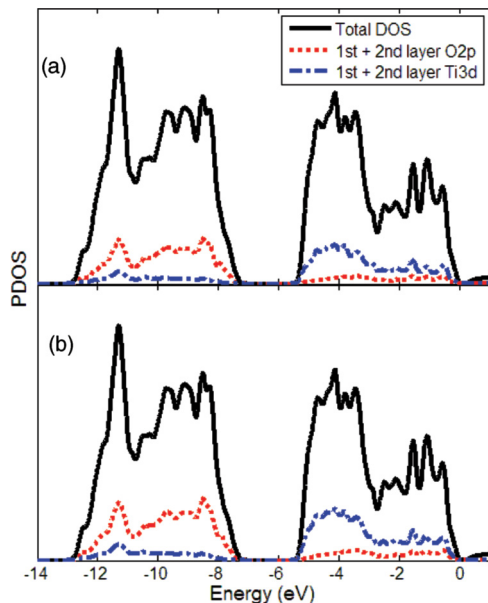


FIG. 5. (Color online) Density of states projected onto the 3d orbitals of Ti and the 2p orbitals of O atoms on both the first and second TiO<sub>2</sub> layers along the horizontal (a) and vertical (b) confinement directions for 6 × 8 nanowire. The zero of the DOS energy scale is the vacuum level. We have also shown the total DOS of the nanowire as a common reference in both figures.

The mixed-parity 5 × 8 nanowire exhibits an interesting spatial separation between the electron and hole states due to the lack of mirror symmetry along the vertical confinement direction, as demonstrated in Fig. 6(B) (similar patterns are also observed in other mixed-parity nanowires). The wave function at the valence-band edge is localized at the top half of the nanowire. Along each confinement direction, the spatial distribution of the wave function is qualitatively similar to that of the 6 × 8 nanowire, with additional contributions from the O-2c atoms at the outermost layers and corners of the nanowire. In contrast, the wave function at the conduction-band edge is localized primarily at the second layer from the bottom facet. Along the horizontal confinement direction, the wave function remains mainly contributed by the 3d orbitals of the surface Ti-5c and the subsurface Ti-6c atoms, with significant mixing with the 2p orbitals of the intermediate O atoms.

The 3 × n nanowires are rather special due to the absence of a surface bilayer when there are only three TiO<sub>2</sub> layers along the first (horizontal) confinement direction (Fig. 7). We find that the opposite tendency for surface Ti-5c and Ti-6c atoms to relax inward and outward is significantly enhanced along the first confinement direction, with the relative displacement between the two types of Ti atoms along the surface normal increased to around 0.25 Å compared to 0.1–0.15 Å in other nanowires. Consequently the nanowire property becomes sensitive to whether the mirror Ti-O layer terminates on the Ti-5c or Ti-6c atoms along the horizontal confinement direction. From the LDOS plots in Fig. 7, we find that the

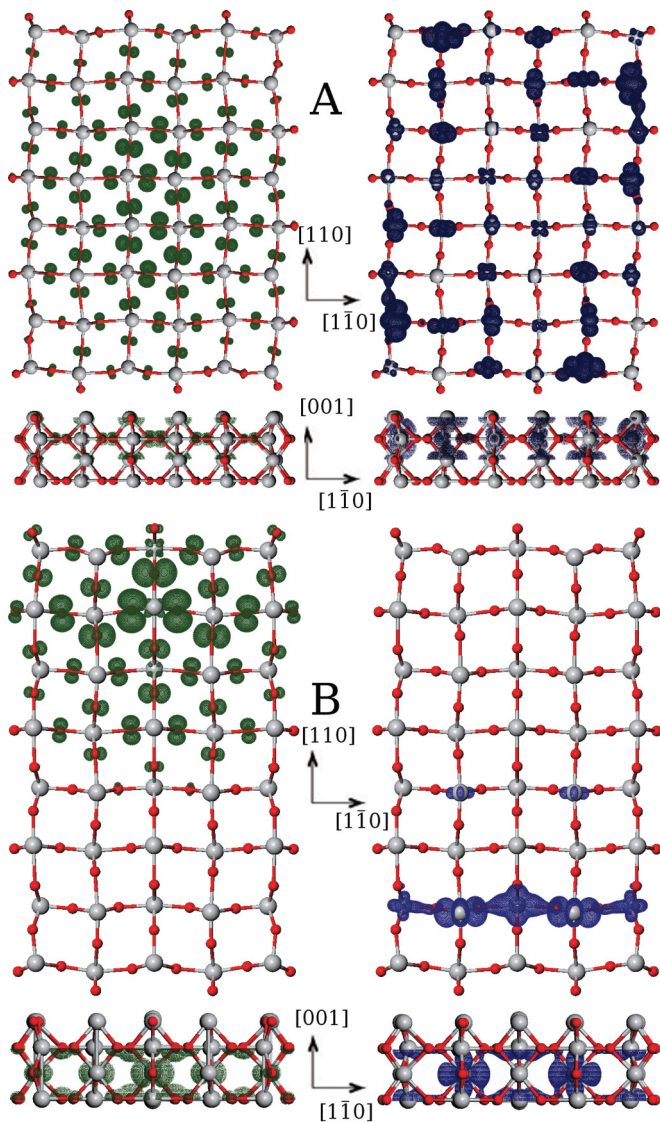


FIG. 6. (Color online) Isosurface plots of the local density of states (LDOS) at the valence-band maximum (left figure) and the conduction-band minimum (right figure) for the  $6 \times 8$  (A) and  $5 \times 8$  (B) rutile  $\text{TiO}_2$  nanowires. The large gray and small red spheres represent Ti and O atoms, respectively. For each nanowire, both the top view (upper figure) and side view (lower figure) of the LDOS are shown.

wave functions at the conduction-band edge for both  $3 \times 7_1$  and  $3 \times 7_2$  nanowires are centered around the Ti-6c atoms on the mirror Ti-O plane, which bridge the two Ti-5c atoms on opposite facets along the horizontal confinement direction with significant mixing with the  $2p$  orbitals of the intermediate O atoms. In contrast, the wave functions at the valence-band edge are contributed by both the surface O-2c atoms and the subsurface O-3c atoms that bridge the Ti-6c atoms on both the mirror Ti-O layer and the opposite facets along the horizontal confinement direction.

Further insights into the nature of bonding within the  $\text{TiO}_2$  nanowires are provided by the crystal orbital overlap population (COOP) plots (Fig. 8). Close to the conduction-band edge of the  $6 \times 8$  nanowire, we find that the overlap

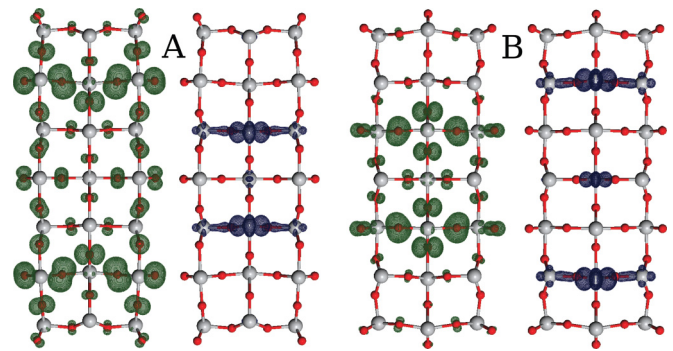


FIG. 7. (Color online) Cross-sectional view of the type-1  $3 \times 7_1$  (A) and type-2  $3 \times 7_2$  (B) nanowires. For each nanowire, we have shown the isosurface plots of the LDOS at the valence-band edge (left figure) and the conduction-band edge (right figure). The type-1  $3 \times 7_1$  nanowire has an indirect gap due to a shift in the valence-band maximum away from the  $\Gamma$  point (empty marker in Fig. 3), while the type-2  $3 \times 7_2$  nanowire has a direct gap at the  $\Gamma$  point (filled marker in Fig. 3).

between the  $3d$  orbitals of the surface Ti-5c and subsurface Ti-6c atoms possess strong antibonding character along both confinement directions. Consequently the conduction-band edge decreases in energy with increasing cross-sectional area as the quantum confinement effect is reduced (Fig. 3). Close to the valence-band edge, we find that the overlaps between the  $3d$  orbitals of the subsurface Ti atoms and the  $2p$  orbitals of the O atoms above (underneath) possess strong bonding (nearly nonbonding) character. This explains the strong coupling between the first and second layers, which in turn are weakly bound to the interior of the nanowires, corroborated by the interlayer distances presented in Table II.

For the mixed-parity  $5 \times 8$  nanowire, we find that the overlap between the  $3d$  orbitals of surface Ti-5c and subsurface Ti-6c atoms remains strongly antibonding from the COOP plot in Fig. 8. Due to the localized nature of the wave function at the conduction-band edge, the quantum confinement effect is effectively reduced. This lowers the conduction-band energy at the  $\Gamma$  point and gives rise to direct band gap. We note that the antibonding character between the surface Ti and O orbitals in the conduction band appears at much lower energy in the horizontal direction than that in the vertical direction, showing that the change in band structure arises from quantum confinement effect along the horizontal direction. Between the  $5 \times n$  and  $7 \times n$  nanowires, we find instead overall similar characteristics in both the LDOS and COOP plots, leading to a qualitatively similar trend in their band structures.

From the COOP plot between the surface Ti and O atoms in Fig. 8, we find the corresponding orbital overlap changes from nonbonding in the indirect-band  $3 \times 7_1$  nanowire to strong antibonding character in the direct-band  $3 \times 7_2$  nanowire close to the conduction-band edge along the second (vertical) confinement direction. Close to the valence-band edge, the corresponding orbital overlap changes from antibonding in the indirect-band  $3 \times 7_1$  nanowire to nonbonding character in the direct-band  $3 \times 7_2$  nanowire (curve d in the corresponding COOP plots of Fig. 8). As the indirect band character of the  $3 \times 7_1$  nanowire is caused by the shift in the VBM away from the  $\Gamma$  point, we analyze in addition the COOP between the

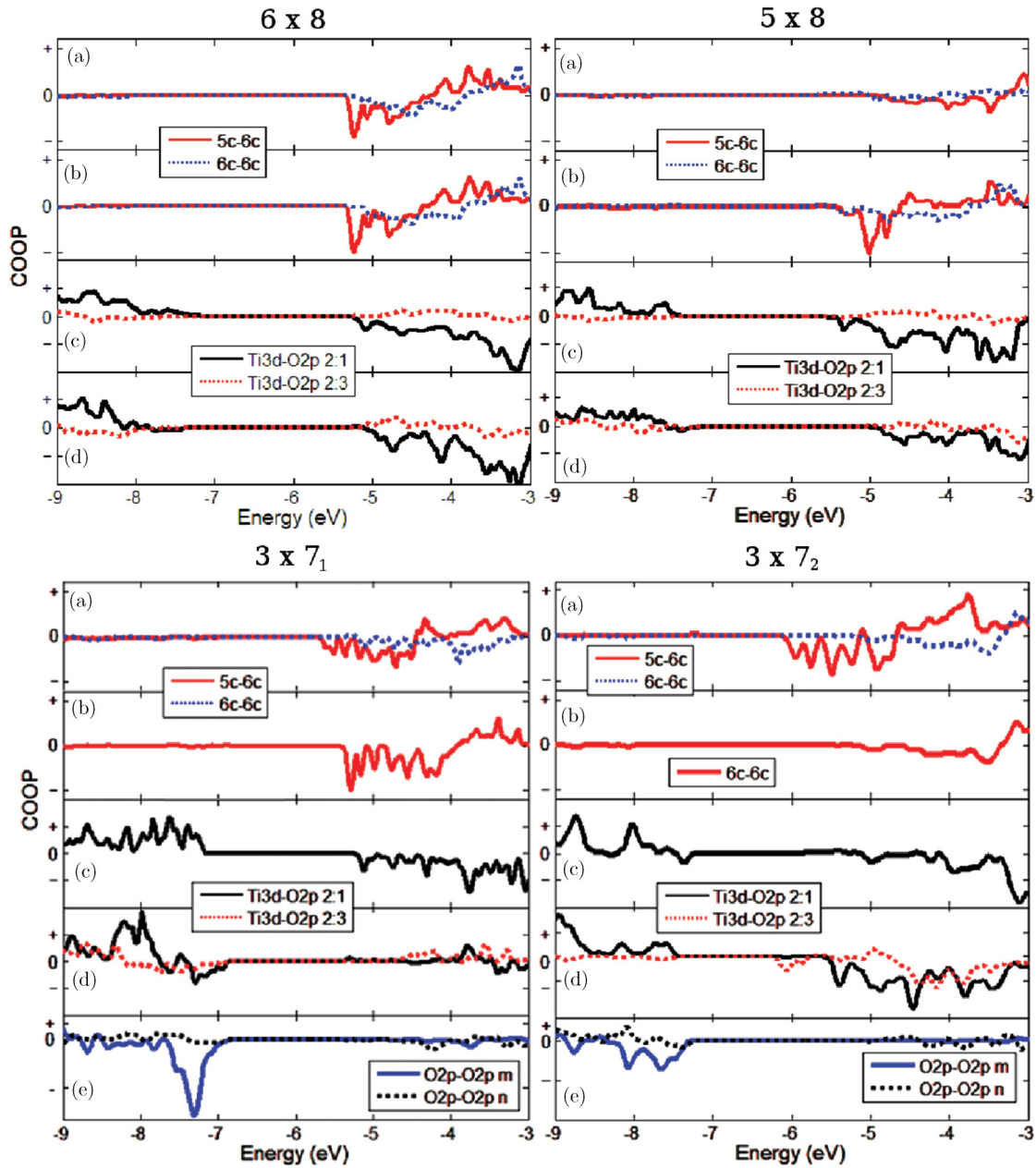


FIG. 8. (Color online) COOP plot for the  $6 \times 8$ ,  $5 \times 8$ ,  $3 \times 7_1$ , and  $3 \times 7_2$   $\text{TiO}_2$  nanowires. For each nanowire, a and b show the COOP between the  $3d$  orbitals of the surface Ti-5c and subsurface Ti-6c atoms (“5c-6c”) and the COOP between the  $3d$  orbitals of the surface and subsurface Ti-6c atoms (“6c-6c”) along both horizontal (a) and vertical (b) confinement directions. c and d show the COOP between the  $3d$  orbitals of the second layer Ti atoms and the  $2p$  orbitals of the O atoms above (“Ti 3d-O 2p 2 : 1”) and the COOP between the  $3d$  orbitals of the second layer Ti atoms and the  $2p$  orbitals of the O atoms underneath (“Ti 3d-O 2p 2 : 3”) along both horizontal (c) and vertical (d) confinement directions. For the two  $3 \times 7$  nanowires, (e) shows the COOP plots between the  $2p$  orbitals of the neighbor O layers along both the horizontal (“O 2p-O 2p m”) and vertical (“O 2p-O 2p n”) confinement directions. The zero of each energy scale is set to the vacuum level.<sup>41</sup>

$2p$  orbitals of the surface and subsurface O atoms (curve e in the corresponding COOP plots of Fig. 8). We find that close to the valence-band edge, the antibonding character between the neighbor O layers is significantly more enhanced in the indirect-band  $3 \times 7_1$  nanowire than that in the direct-band  $3 \times 7_2$  nanowire along the horizontal confinement direction. Since the indirect and direct gaps differ by less than 0.03 eV in the  $3 \times 7_1$  nanowire, the different effects arising from quantum confinement along both directions are sufficient to

change the band characters between the two types of  $3 \times 7$  nanowires.

#### IV. CONCLUSION

In this paper we have analyzed the atomic and electronic properties of the rectangular rutile  $\text{TiO}_2$  nanowires oriented along the [001] direction and enclosed by {110} facets. We find that the dependence of the nanowire properties on the

number of TiO<sub>2</sub> layers is largely connected to the presence or absence of a mirror Ti-O plane along each confinement direction. Although this dependence on the even-odd parity of the number of TiO<sub>2</sub> layers has been discussed in previous studies on rutile TiO<sub>2</sub>(110) thin films and surfaces, we find that the ability to tune separately the number of layers in each confinement direction leads to interesting size- and shape-dependent electronic properties in rutile TiO<sub>2</sub> nanowires, which arise from the interplay between surface relaxation and quantum confinement effects.

We have focused exclusively on stoichiometric nanowires that can be constructed directly from the bulk rutile TiO<sub>2</sub> crystals. In contrast, most of the interesting catalytic properties in rutile TiO<sub>2</sub> are connected with the presence of oxygen vacancy on the (110) surfaces.<sup>1-3</sup> In addition, it would be interesting to understand how the properties of TiO<sub>2</sub> nanowires may be modified by surface functionalization, which invariably occurs in realistic growth and fabrication environment. In this context, a recent study has shown<sup>9</sup> that small-diameter rutile

TiO<sub>2</sub> nanowires with pseudohydrogen passivation may exhibit direct band gap for different sizes and cross-section shapes. Previous work on rutile TiO<sub>2</sub>(110) surfaces has also shown that adding pseudohydrogen passivation in the bottom layer leads to significant suppression of the even-odd oscillation effect.<sup>23</sup> We plan to address these and other interesting questions in future works.

#### ACKNOWLEDGMENTS

This work was partially supported by the New York State Energy Research and Development Authority (NYSERDA). Computations were performed at the UAlbany Research Computing Grid and at the Cornell Nanoscale Science and Technology Facility (CNF) through the support of the Computation Portal of the National Nanotechnology Infrastructure Network (NNIN/C). We thank Derek Stewart of NNIN/C for help.

\*yxue@albany.edu

<sup>1</sup>U. Diebold, *Surf. Sci. Rep.* **48**, 53 (2003).

<sup>2</sup>C. L. Pang, R. Lindsay, and G. Thornton, *Chem. Soc. Rev.* **37**, 2328 (2008).

<sup>3</sup>C. Sun, L.-M. Liu, A. Selloni, G. Q. M. Lu, and S. C. Smith, *J. Mater. Chem.* **20**, 10319 (2010).

<sup>4</sup>A. Kolmakov and M. Moskovits, *Annu. Rev. Mater. Res.* **34**, 151 (2004).

<sup>5</sup>X. Feng, K. Shankar, O. K. Varghese, M. Paulose, T. J. Latempa, and C. A. Grimes, *Nano Lett.* **8**, 3781 (2008).

<sup>6</sup>C. Liu and S. Yang, *ACS Nano* **3**, 1025 (2009).

<sup>7</sup>S. Meng, J. Ren, and E. Kaxiras, *Nano Lett.* **8**, 3266 (2008).

<sup>8</sup>D. Zhang, P. Liu, and C. Liu, *J. Phys. Chem. C* **112**, 16729 (2008).

<sup>9</sup>H. Peng and J. Li, *J. Phys. Chem. C* **112**, 20241 (2008).

<sup>10</sup>D. N. Tafen and J. P. Lewis, *Phys. Rev. B* **80**, 014104 (2009).

<sup>11</sup>D. Çakır and O. Gülseren, *Phys. Rev. B* **80**, 125424 (2009).

<sup>12</sup>D. B. Migas, V. L. Shaposhnikov, V. E. Borisenko, and F. Arnaud D'Avitaya, *J. Phys. Chem. C* **114**, 21013 (2010).

<sup>13</sup>A. Iacomino, G. Cantele, F. Trani, and D. Ninno, *J. Phys. Chem. C* **114**, 12389 (2010).

<sup>14</sup>T. He, Z. S. Hu, J. L. Li, and G. W. Yang, *J. Phys. Chem. C* **115**, 13837 (2011).

<sup>15</sup>B. Aradi, P. Deák, H. A. Huy, A. Rosenauer, and T. Frauenheim, *J. Phys. Chem. C* **115**, 18494 (2011).

<sup>16</sup>T. Bredow, L. Giordano, F. Cinquini, and G. Pacchioni, *Phys. Rev. B* **70**, 035419 (2004).

<sup>17</sup>M. Ramamoorthy, D. Vanderbilt, and R. D. King-Smith, *Phys. Rev. B* **49**, 16721 (1994).

<sup>18</sup>S. Bates, G. Kresse, and M. Gillan, *Surf. Sci.* **385**, 386 (1997).

<sup>19</sup>P. J. D. Lindan, N. M. Harrison, M. J. Gillan, and J. A. White, *Phys. Rev. B* **55**, 15919 (1997).

<sup>20</sup>S. J. Thompson and S. P. Lewis, *Phys. Rev. B* **73**, 073403 (2006).

<sup>21</sup>K. J. Hameeuw, G. Cantele, D. Ninno, F. Trani, and G. Iadonisi, *J. Chem. Phys.* **124**, 024708 (2006).

<sup>22</sup>A. Kiejna, T. Pabisiak, and S. W. Gao, *J. Phys.: Condens. Matter* **18**, 4207 (2006).

<sup>23</sup>P. M. Kowalski, B. Meyer, and D. Marx, *Phys. Rev. B* **79**, 115410 (2009).

<sup>24</sup>J. M. Soler, E. Artacho, J. D. Gale, A. García, J. Junquera, P. Ordejón, and D. Sánchez-Portal, *J. Phys.: Condens. Matter* **14**, 2745 (2002).

<sup>25</sup>N. Troullier and J. L. Martins, *Phys. Rev. B* **43**, 1993 (1991).

<sup>26</sup>J. P. Perdew, K. Burke, and M. Ernzerhof, *Phys. Rev. Lett.* **77**, 3865 (1996).

<sup>27</sup>J. P. Perdew and A. Zunger, *Phys. Rev. B* **23**, 5048 (1981).

<sup>28</sup>ATOM, a program for DFT calculations in atoms and pseudopotential generation, distributed as part of the SIESTA software package. See [<http://www.icmab.es/siesta/atom>].

<sup>29</sup>W. Press, S. Teukolsky, W. Vetterling, and B. Flannery, *Numerical Recipes in FORTRAN: The Art of Scientific Computing*, 2nd ed. (Cambridge University Press, Cambridge, England, 1992).

<sup>30</sup>S. Garcia-Gil, A. Garcia, N. Lorente, and P. Ordejón, *Phys. Rev. B* **79**, 075441 (2009).

<sup>31</sup>H. J. Monkhorst and J. D. Pack, *Phys. Rev. B* **13**, 5188 (1976).

<sup>32</sup>J. K. Burdett, T. Hughbanks, G. J. Miller, J. W. Richardson, and J. V. Smith, *J. Am. Chem. Soc.* **109**, 3639 (1987).

<sup>33</sup>V. Jeanne-Rose and B. Poumellec, *J. Phys.: Condens. Matter* **11**, 1123 (1999).

<sup>34</sup>F. Labat, P. Baranek, C. Domain, C. Minot, and C. Adamo, *J. Chem. Phys.* **126**, 154703 (2007).

<sup>35</sup>B. Hamad, *Eur. Phys. J. B* **70**, 163 (2009).

<sup>36</sup>A. Amtout and R. Leonelli, *Phys. Rev. B* **51**, 6842 (1995).

<sup>37</sup>A. K. See and R. A. Bartynski, *Phys. Rev. B* **50**, 12064 (1994).

<sup>38</sup>*A Primer in Density Functional Theory*, edited by C. Fiohais, F. Noqueira, and M. Marques (Springer, Berlin, 2003).

<sup>39</sup>W. G. Aulbur, L. Jonsson, and J. W. Wilkins, *Solid State Phys.* **54**, 1 (1999).

<sup>40</sup>W. Kang and M. S. Hybertsen, *Phys. Rev. B* **82**, 085203 (2010).

<sup>41</sup>J. Junquera, M. Zimmer, P. Ordejón, and P. Ghosez, *Phys. Rev. B* **67**, 155327 (2003).

<sup>42</sup>J. F. Justo, R. D. Menezes, and L. V. C. Assali, *Phys. Rev. B* **75**, 045303 (2007).

<sup>43</sup>R. Hoffmann, *Rev. Mod. Phys.* **60**, 601 (1988).